RSC Advances



PAPER

View Article Online
View Journal | View Issue



Cite this: *RSC Adv.*, 2025, **15**, 22690

# Fabrication of inorganic@organic $V_2O_5$@PEDOT nanocomposite cathode for advanced aqueous manganese-ion batteries†

Xianyu Liu, *[a] Jianan Zhao,[b] Zhigang Fan,*[c] Yingchun Xiao,[a] Yande Zhao[a] and Qing Guo[a]

Received 8th May 2025
Accepted 19th June 2025

DOI: 10.1039/d5ra03230j

rsc.li/rsc-advances

Aqueous manganese-ion batteries (AMIBs) show promise for energy storage because Mn anodes exhibit high capacity (976 mAh $g^{-1}$) and low potential (−1.18 V *vs.* SHE). However, cathode development faces challenges due to solvated $Mn^{2+}$ with a large radius, resulting in slow ion diffusion, structural instability and limited capacity. Herein, we synthesized inorganic@organic $V_2O_5$@PEDOT nanocomposite *via* a facile *in situ* polymerization method by combining the EDOT monomer with $V_2O_5$. The resulting PEDOT coating exhibited strong adhesion to the $V_2O_5$ substrate owing to the redox reaction at the organic–inorganic interface, creating a unique hybrid architecture with enhanced charge transfer properties. Furthermore, the PEDOT composite significantly enhanced electrochemical performance by simultaneously suppressing vanadium dissolution and improving electronic conductivity, resulting in exceptionally high specific capacity (340.3 mAh $g^{-1}$ at 0.5 A $g^{-1}$) and rate capability (211.8 mAh $g^{-1}$ at 5 A $g^{-1}$). Systematic mechanism characterization confirmed the structural stability and high reversibility of $Mn^{2+}$ insertion/extraction. The practical applicability of the nanocomposite was further demonstrated in a full-cell configuration (Mn‖$V_2O_5$@PEDOT), demonstrating high capacity. This study presents a high-performance cathode material for advanced AMIBs and provides new insights into design principles.

## 1. Introduction

Aqueous battery systems have emerged as promising candidates for large-scale energy storage applications primarily because of their inherent safety features and environmental advantages.[1–3] Among the various aqueous battery technologies, manganese (Mn) metal stands out because of its low redox potential (−1.18 V *vs.* standard hydrogen electrode), suggesting that aqueous manganese-ion batteries (AMIBs) can achieve higher operating voltages.[4] Furthermore, Mn anodes offer additional advantages, including abundant natural reserves, low costs, nontoxicity, and high capacity (976 mAh $g^{-1}$ based on the Mn/$Mn^{2+}$ redox couple), positioning AMIBs as highly competitive candidates for next-generation aqueous rechargeable batteries.[5,6] The electrochemical performance of AMIBs is largely governed by their cathode materials. Current research has focused on three major categories of cathode materials: vanadium-based compounds, manganese-based oxides and organic materials.[7–9]

Among these cathode materials, vanadium-based materials have attracted particular attention owing to their cost-effectiveness, multivalent oxidation states, and high theoretical capacities.[10,11] Nevertheless, the practical application of $V_2O_5$-based cathodes is limited by sluggish reaction kinetics and rapid capacity fading due to poor electrical conductivity, strong $Mn^{2+}$ electrostatic interactions, and material dissolution issues.[12–14] To address these technical challenges, research efforts have been devoted to developing effective modification strategies, which primarily focus on defect engineering,[15] heteroatom doping,[16,17] conductive network construction[18,19] and electrolyte optimization.[20,21] These modification approaches synergistically enhance electrochemical performance by simultaneously improving charge transfer kinetics, structural stability, and interfacial compatibility.[22] For instance, $Al^{3+}$ was introduced as a pillar in layered $V_2O_5$ to develop an AlVO cathode *via* facile one-step hydrothermal synthesis, demonstrating exceptional compatibility with AMIBs. This cathode material exhibited remarkable electrochemical properties and rapid reaction kinetics.[5] However, metal-ion-intercalated $V_2O_5$ electrodes typically exhibit poor electronic conductivity, which significantly limits their electrochemical performance. Moreover, conducting poly(3,4-ethylenedioxythiophene) (PEDOT) has been widely employed

[a]Bailie School of Petroleum Engineering, Lanzhou City University, Lanzhou 730070, China. E-mail: xyliu15@mail.ustc.edu.cn

[b]Department of Materials Science and Engineering, College of Transportation Engineering, Dalian Maritime University, Dalian, 116026, PR China

[c]National Petroleum and Natural Gas Pipeline Network Group Co., Ltd, Yunnan Branch, Kunming 650032, China. E-mail: fengdediaolin@163.com

† Electronic supplementary information (ESI) available. See DOI: https://doi.org/10.1039/d5ra03230j

as an electrode material in energy storage systems because of its relatively high conductivity.[23,24] PEDOT has emerged as an ideal candidate for enhancing the electrical conductivity of composite materials because of its excellent compatibility with inorganic materials. The incorporation of PEDOT can significantly improve the overall performance of electrode materials by optimizing electron conduction pathways.[25,26] PEDOT polymers can be incorporated into $V_2O_5$ to fabricate inorganic@organic nanocomposites, significantly enhancing the stable host structures.

In this study, we develop an inorganic@organic $V_2O_5$@PEDOT nanocomposite *via* an *in situ* polymerization approach utilizing the interfacial redox reaction between $V_2O_5$ and the EDOT monomer at room temperature. The *in situ* formed PEDOT chains form conductive networks and mixed $V^{5+}/V^{4+}$ valences, which significantly improve the electronic conductivity and ionic diffusion coefficients for AMIBs. Benefiting from these synergistic effects, the as-prepared inorganic@organic $V_2O_5$@PEDOT nanocomposite manifests exceptional electrochemical performance, including a high capacity of 340 mAh $g^{-1}$ at 0.5 A $g^{-1}$, a remarkable rate capability (maintaining 211.8 mAh $g^{-1}$ at 5 A $g^{-1}$) and outstanding cycling stability after 1000 cycles in an $MnSO_4$ electrolyte. This approach demonstrates exceptional potential for practical applications, combining facile synthesis with outstanding electrochemical performance.

## 2. Experimental section

### 2.1 Material preparation

Initially, 7 g of a $V_2O_5$ powder was dispersed in 70 mL of deionized water under continuous stirring at room temperature to form a homogeneous suspension. Subsequently, 3 mL of the EDOT monomer was added to the system drop-wise, followed by continuous stirring for 144 h at room temperature. During this process, a distinct color transition from yellow to green was observed, indicating the occurrence of polymerization. The resultant $V_2O_5$@PEDOT products were obtained *via* vacuum-drying at 80 °C for 15 h.

### 2.2 Material characterization

The crystalline phases and structural properties of the synthesized $V_2O_5$@PEDOT were characterized by X-ray diffraction (XRD) using a Rigaku D-Max-3A diffractometer with Cu Kα radiation ($\lambda = 1.5418$ Å). Morphological analysis was performed by scanning electron microscopy (SEM; Zeiss SUPRA 55 SAPPHIRE) and transmission electron microscopy (TEM; JEM2100F). The chemical compositions and surface electronic states were investigated by X-ray photoelectron spectroscopy (XPS) on a PerkinElmer PHI 1600 ESCA system equipped with an Al Kα X-ray source.

### 2.3 Electrochemical measurement

The carbon anodes were prepared by formulating uniform slurries containing activated carbon (AC), conductive carbon, and a PVDF binder in an optimized weight ratio (8 : 1 : 1) using NMP as the processing solvent. These slurries were precisely coated onto a carbon felt, followed by drying at 80 °C, achieving controlled active material loadings of ∼20 mg $cm^{-2}$. The cathodes were prepared by combining $V_2O_5$@PEDOT composites with carbon nanotubes (CNTs) at a ratio of 7 : 3 and dispersed in DMF. The mixed solution underwent ultrasonic treatment for 30 min to ensure homogeneous dispersion. Then, the $V_2O_5$@PEDOT composites were obtained *via* filtration. The weight loading of $V_2O_5$@PEDOT was ∼1.5 mg $cm^{-2}$. For the cell assembly, 2032-type coin cells were configured using either polished Mn metal sheets or carbon felt as anodes, with multiple filter paper separators (diameter = 16 mm) and an aqueous $MnSO_4$ electrolyte (3 M). The electrochemical performance was comprehensively evaluated *via* cyclic voltammetry (0.5–2.5 mV $s^{-1}$ scan rates) and galvanostatic charge–discharge tests within appropriate voltage windows (−1.4 to 0.8 V for AC‖$V_2O_5$; 0.4–1.9 V for Mn‖$V_2O_5$@PEDOT) using analysis equipment (CHI 660E workstation and LAND CT2001A system, respectively).

## 3. Results and discussion

To elucidate the structure–property relationship of the $V_2O_5$@PEDOT composite, SEM and TEM were employed for morphological investigations. As evidenced in Fig. 1a–c, the composite maintains a well-defined nanorod-like architecture, exhibiting uniform widths of approximately 30 nm with longitudinal dimensions extending to several micrometers. After composting with CNTs, $V_2O_5$@PEDOT is embedded within the 3D interconnected CNT network (Fig. 1d–f). The CNT matrix fully encapsulates $V_2O_5$ nanorods, forming a robust conductive framework that ensures stable interfacial contact between the active material and conductive substrate. This hierarchical architecture facilitates efficient charge transfer pathways, thereby optimizing electrochemical kinetics.[27] Further SEM-EDS mapping (Fig. S1a and b†) reveals the homogeneous distribution of C, V, O, and S, confirming the uniform incorporation of PEDOT across the composite. The oxidative polymerization process is initiated when EDOT monomers come into contact with $V_2O_5$ in the aqueous medium, leading to the *in situ* formation of a conductive PEDOT layer on the $V_2O_5$ surface. As shown in Fig. S2,† the content of PEDOT is ∼16.3%. This interfacial reaction occurs *via* a well-defined redox mechanism, in which $V_2O_5$ serves as the oxidizing agent and structural template. Thus, bulk $V_2O_5$ is exfoliated into the nanorod-like morphology.[28] XRD analysis was performed to investigate the structural evolution of the $V_2O_5$@PEDOT composite (Fig. 2a). The diffraction patterns confirm that the phase of $V_2O_5$ (JCPDS no. 41-1426) remains intact after PEDOT modification (Fig. S3†). Importantly, the (200) diffraction peak exhibits a notable shift from 15.3° in pristine $V_2O_5$ to 9.1° in the $V_2O_5$@PEDOT composite, accompanied by peak broadening and intensity reduction. According to Bragg's law calculations, this shift corresponds to an interlayer spacing expansion from 5.8 Å to 9.7 Å, providing direct evidence of the successful PEDOT intercalation and the resulting interlayer expansion effect.[24] Furthermore, intercalated PEDOT molecules serve as structural

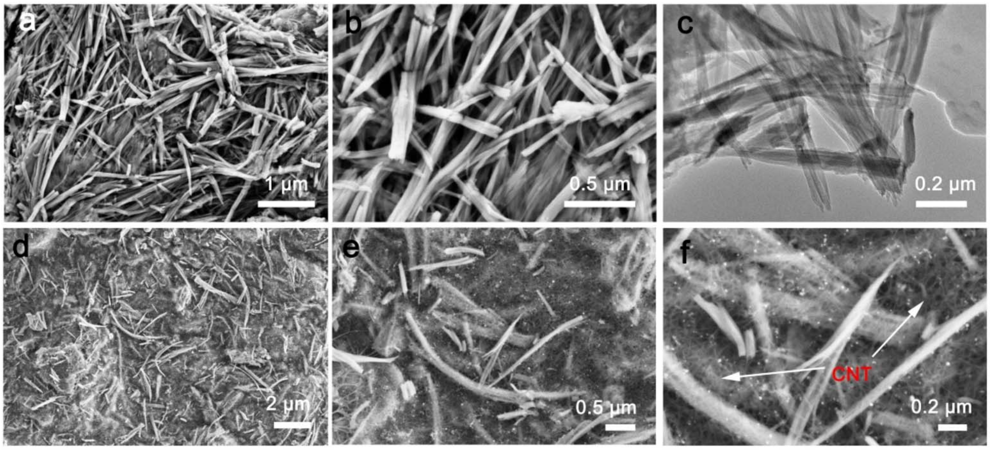


Fig. 1 (a and b) SEM image and (c) TEM image of $V_2O_5$@PEDOT. (d–f) SEM images of $V_2O_5$@PEDOT composites with CNTs.

pillars that effectively prevent the collapse of the layered structure during electrochemical cycling.[29]

The XPS spectrum of the $V_2O_5$@PEDOT composite is presented in Fig. 2b. Survey scan analysis reveals distinct characteristic peaks corresponding to C 1s, S 2p, V 2p, and O 1s core levels, confirming the successful incorporation of PEDOT into the composite. The high-resolution V 2p spectrum (Fig. 2c) exhibits a doublet structure with binding energies of 516.2 eV (V $2p_{3/2}$) and 525.0 eV (V $2p_{1/2}$), which demonstrates the coexistence of $V^{5+}/V^{4+}$ mixed valence states in the composite.[25] This valence state analysis indicates that the interfacial interaction between $V_2O_5$ and PEDOT induces the partial reduction of $V^{5+}$ to $V^{4+}$, and the resulting mixed valence configuration significantly enhances the $Mn^{2+}$ transport kinetics during electrochemical processes.[30] The S 2p spectrum (Fig. 2d) displays characteristic features of the thiophene-based PEDOT polymer. These spectroscopic signatures provide compelling evidence of the successful polymerization of EDOT and its effective integration into the $V_2O_5$ matrix. Based on the XRD and XPS results of the $V_2O_5$@PEDOT composite, the reaction mechanism between $V_2O_5$ and PEDOT is discussed in detail. This study proposes a simple *in situ* polymerization method based on the redox reaction between $V_2O_5$ and the EDOT monomer. $V_2O_5$ acts as an oxidizing agent, initiating electron transfer and the

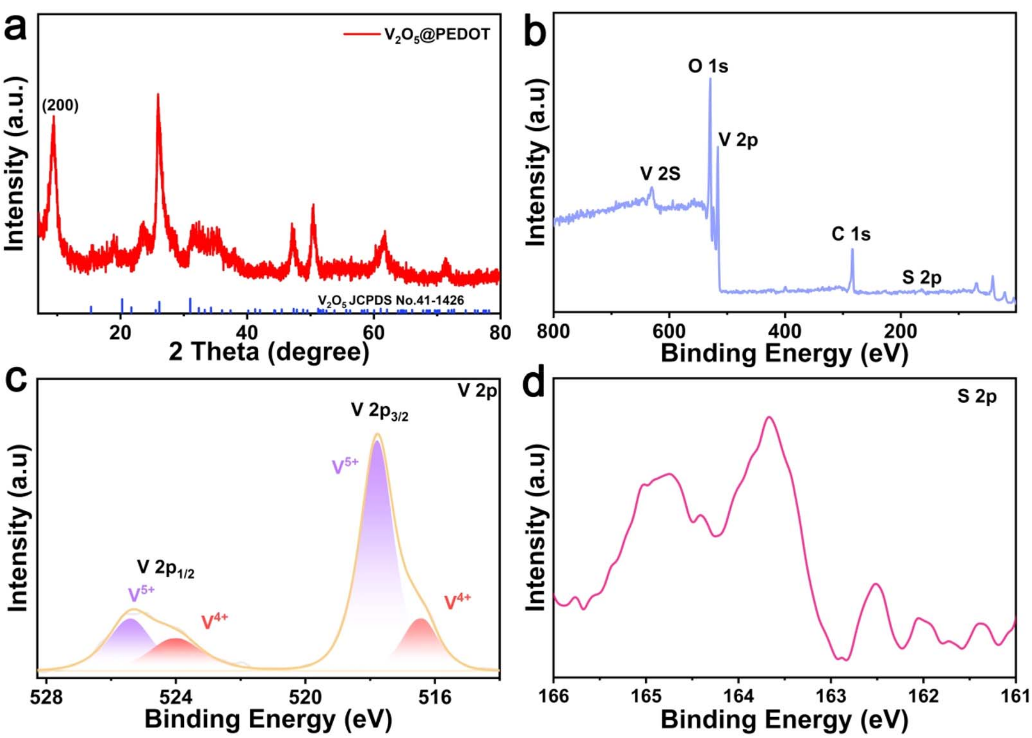


Fig. 2 (a) XRD pattern, (b) XPS spectrum, (c) V 2p spectrum and (d) S 2p spectrum of the $V_2O_5$@PEDOT composite.

deprotonation of EDOT monomers. This redox process involves oxygen extraction from the $V_2O_5$ lattice at the interface, leading to the reduction of $V^{5+}$ to $V^{4+}$ (as confirmed by XPS V 2p analysis in Fig. 2c) while simultaneously promoting EDOT polymerization into PEDOT on $V_2O_5$. After PEDOT polymerization, the (200) diffraction peak exhibits a notable shift to a high degree in the $V_2O_5$@PEDOT composite (Fig. 2a), providing direct evidence of the successful PEDOT intercalation and the resulting interlayer expansion effect.[24] The resulting PEDOT coating exhibits strong adhesion to the $V_2O_5$ substrate at the organic–inorganic interface, creating a unique hybrid architecture with enhanced charge transfer properties.[31]

Coin cells were assembled using the AC anodes and 3 M $MnSO_4$ electrolyte for comparing the performance of $V_2O_5$@PEDOT composite cathodes. As shown in Fig. 3a, the composite cathode exhibits similar charge–discharge voltage plateaus at 0.5 A $g^{-1}$, demonstrating excellent electrochemical reversibility. Rate capability analysis (Fig. 3b) reveals that the optimized $V_2O_5$@PEDOT cathode delivers superior specific capacities of 340.3, 297.4, 242.3, and 211.8 mAh $g^{-1}$ at various current densities. The capacity significantly outperforms unmodified $V_2O_5$ (143.1 mAh $g^{-1}$ at 5 A $g^{-1}$). Remarkably, when the current density is returned to 0.5 A $g^{-1}$ after high-rate testing, $V_2O_5$@PEDOT maintains 291.2 mAh $g^{-1}$, demonstrating exceptional $Mn^{2+}$ storage reversibility and rapid ion transport kinetics. This was further confirmed by the well-defined charge–discharge plateaus and reduced polarization observed at various current densities (Fig. 3c). Long-term cycling tests at 1 A $g^{-1}$ (Fig. 3d) show that the $V_2O_5$@PEDOT nanocomposite cathode achieves an initial capacity of 328.9 mAh $g^{-1}$, which is much higher than that of $V_2O_5$. Furthermore, the $V_2O_5$@PEDOT nanocomposite maintains 176.4 mAh $g^{-1}$ at 5 A $g^{-1}$ after 1000 cycles (Fig. 3e), demonstrating outstanding structural stability in the $MnSO_4$ electrolyte. The stable cycle performance can also be proven by EIS measurements. After 100 cycles at 1.0 A $g^{-1}$, the $R_{ct}$ of the $V_2O_5$@PEDOT electrodes is 7.2 Ω (Fig. S4†). The $R_{ct}$ after cycling is similar to that before cycling (7.5 Ω). This means that ion transport is stable during cycling.

To elucidate the electrochemical kinetics of the $V_2O_5$@PEDOT composite, CV measurements were systematically performed across a range of scan rates (0.5–2.5 mV $s^{-1}$), as presented in Fig. 4a and S5.† The CV profiles exhibit well-defined redox peaks with maintained shape integrity across scan rates, demonstrating the electrochemical reversibility of the $V_2O_5$@PEDOT nanocomposite. The kinetic behavior was quantitatively analyzed using the relationship between the peak current ($i$) and scan rate ($\nu$):[32,33]

$$i = a\nu^b$$

where the $b$-value serves as a critical indicator of the charge storage mechanism. $b = 0.5$ suggests a diffusion-controlled process. $b = 1.0$ indicates surface-controlled capacitive storage. The kinetic analysis of the $V_2O_5$@PEDOT nanocomposite cathode reveals a mixed charge storage mechanism, as evidenced by the calculated $b$-values of 0.85 (peak I), 0.71 (peak II), 0.81 (peak III), and 0.88 (peak IV) derived from scan-rate-dependent CV measurements (Fig. 4b). These intermediate $b$-values between 0.5 and 1.0 suggest that the electrochemical reactions are governed by a combination of diffusion-controlled intercalation and surface-mediated pseudocapacitive processes.

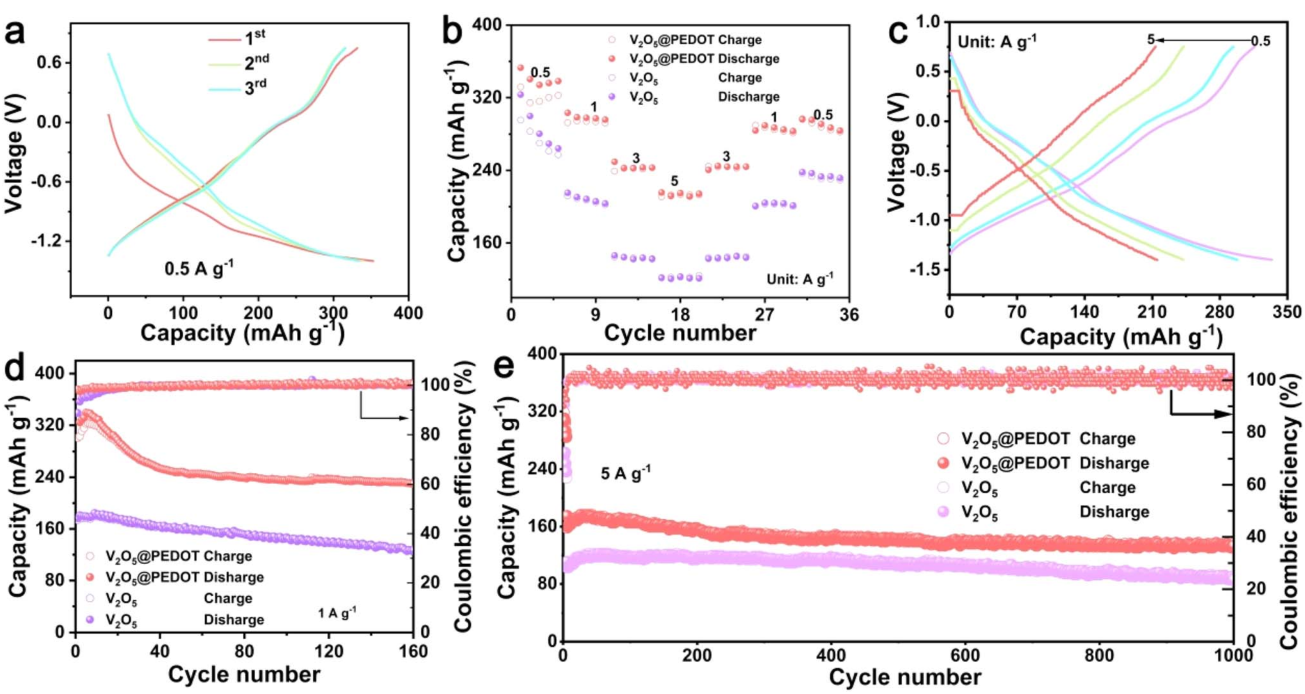


Fig. 3 (a) Initial three charge–discharge cycles, (b) rate performance, (c) charge–discharge curves, (d) cycle life at 1 A $g^{-1}$ and (e) cycle life at 5 A $g^{-1}$ of the $V_2O_5$@PEDOT composite.

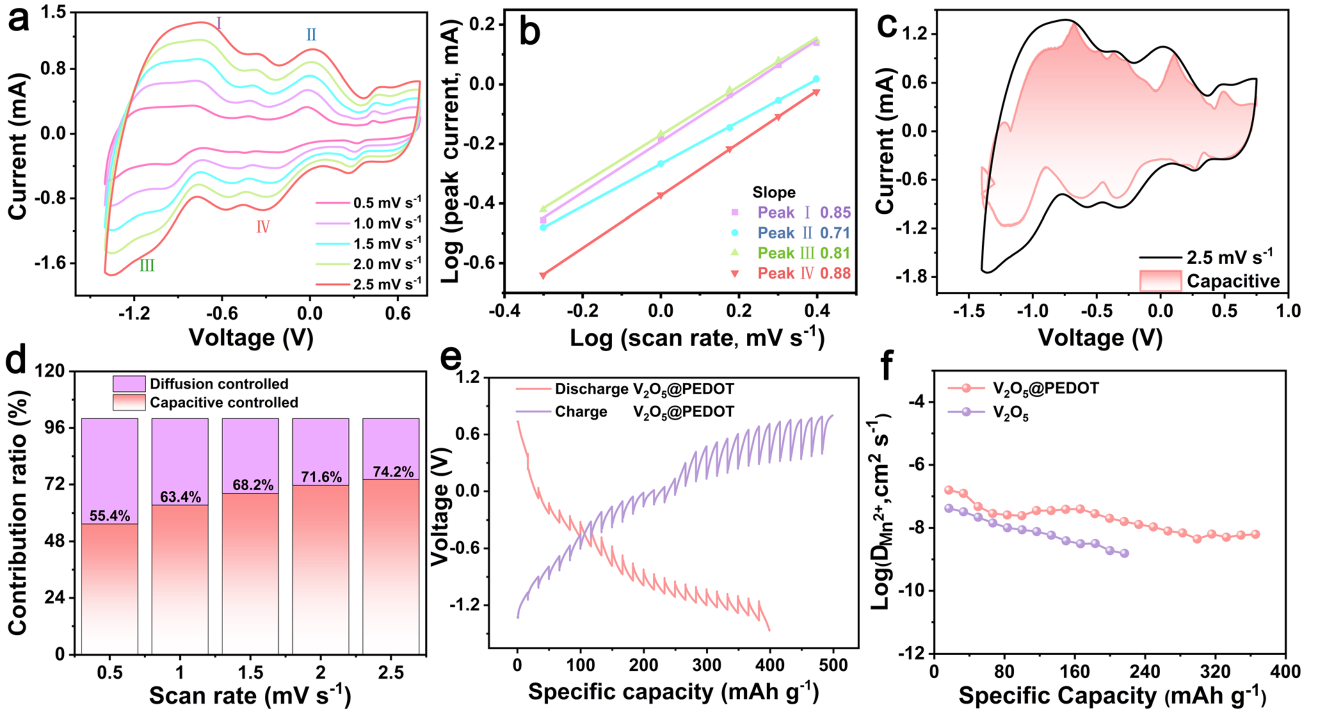


Fig. 4 (a) CV curves, (b) log($i$) *vs.* log($\nu$), (c) capacitive contribution, (d) capacitive contribution at 2.5 mV $s^{-1}$, (e) the GCD curve of GITT, and (f) the relevant $Mn^{2+}$ ion diffusion coefficient of the $V_2O_5$@PEDOT composite.

The quantitative separation of capacitive- and diffusion-controlled contributions can be achieved using the following equation:[34,35]

$$i = k_1\nu + k_2\nu^{\frac{1}{2}}$$

Electrochemical kinetic analysis reveals a distinct evolution in the charge storage behavior of the $V_2O_5$@PEDOT cathode with increasing scan rates (0.5–2.5 mV $s^{-1}$). As shown in Fig. 4c, the capacitive contribution percentage demonstrates a progressive increase from 55.4% to 74.2%, reaching its maximum at a scan rate of 2.5 mV $s^{-1}$ (Fig. 4d). This trend contrasts markedly with the $V_2O_5$ cathode, which exhibits low *b*-values (Fig. S6†) and decreased capacitive contributions (Fig. S7†). These findings demonstrate that the inorganic@organic $V_2O_5$@PEDOT nanocomposite architecture effectively promotes surface-controlled charge storage processes. The $Mn^{2+}$ diffusion coefficient was quantitatively analyzed using the galvanostatic intermittent titration technique (GITT). As illustrated in Fig. 4e, the linear correlation between the voltage change ($\Delta E_\tau$) and $\tau^{1/2}$, where $\tau$ is pulse duration, enabled the calculation of $Mn^{2+}$ diffusion coefficients ($D_{Mn^{2+}}$) using the equation:

$$D_{Mn^{2+}} = \frac{4}{\tau\pi}\left(\frac{m_B V_m}{M_B S}\right)^2\left[\frac{\Delta E_s}{\Delta E_\tau}\right]^2 (\tau \ll L^2/D_{Mn})$$

The GITT parameters are defined as follows: $\tau$ is the pulse time, $m_B$ is the active mass, $M_B$ is the molar mass, $V_m$ is the molar volume, and $\Delta E_s$ is the equilibrium voltage change. The $V_2O_5$@PEDOT cathode demonstrates significantly enhanced kinetics, with $D_{Mn^{2+}}$ values between $1.56 \times 10^{-7}$ $cm^2$ $s^{-1}$ and $4.46 \times 10^{-9}$ $cm^2$ $s^{-1}$ (Fig. 4f), which are better than those of pristine $V_2O_5$ ($4.21 \times 10^{-8}$ $cm^2$ $s^{-1}$ to $1.55 \times 10^{-9}$ $cm^2$ $s^{-1}$).

Using a combination of *ex situ* XRD and XPS analyses, the structural dynamics and charge storage mechanism of the $V_2O_5$@PEDOT cathode during the electrochemical process were systematically elucidated (Fig. 5a). As depicted in Fig. 5b, the (200) diffraction peak shifts toward lower angles during the discharging process, corresponding to an interlayer expansion induced by $Mn^{2+}$ intercalation. Notably, the peak fully reverts to its initial position upon charging to 0.8 V, demonstrating exceptional structural reversibility and lattice stability (Fig. 5c).[36] Complementary XPS analysis (Fig. 5d) reveals the redox chemistry underlying this process: the pristine electrode exhibits mixed $V^{5+}$ (517.6/525.2 eV) and $V^{4+}$ (516.2/523.6 eV) states due to partial reduction during PEDOT polymerization. Upon discharging to −1.4 V, the emergence of $V^{3+}$ species and the enhancement of $V^{4+}$ signals confirm $Mn^{2+}$ intercalation, while recharging restores the dominant $V^{5+}$ state, verifying the presence of the highly reversible vanadium redox (Fig. 5e). Concurrently, the Mn 2p spectra show clear $Mn^{2+}$ signals in the discharged state, with residual intensity persisting in the charged state, corroborating the XRD observations of incomplete $Mn^{2+}$ extraction. These findings collectively establish a $Mn^{2+}$ intercalation/deintercalation mechanism with minor irreversibility (Fig. 5f). The spatial distribution and electrochemical evolution of elemental constituents in the $V_2O_5$@PEDOT cathode were thoroughly investigated using SEM-EDS. As illustrated in Fig. S8,† EDS elemental mapping demonstrates that V, O, and S exhibit nearly identical spatial distribution patterns in discharged (Fig. S8a†) and charged (Fig. S8b†) states, confirming exceptional structural stability during electrochemical cycling. Mn exhibits pronounced state-dependent behavior, with strong characteristic signals appearing during discharging and a significantly attenuated intensity appearing upon charging, which provides direct evidence of the $Mn^{2+}$ intercalation/deintercalation mechanism. The $Mn^{2+}$ intercalation/deintercalation mechanism is schematically shown in Fig. 6. According to *ex situ* XRD and XPS analyses, $Mn^{2+}$ ions are intercalated into the $V_2O_5$@PEDOT electrodes in the discharged state. After the charging process, $Mn^{2+}$ ions are deintercalated from the $V_2O_5$@PEDOT electrodes.

Building on the outstanding performance of AC$\|V_2O_5$@PEDOT cells, we further investigated the practical application potential of $V_2O_5$@PEDOT cathodes in manganese-ion full battery systems by pairing them directly with Mn metal anodes. The Mn$\|V_2O_5$@PEDOT full cell demonstrates remarkable electrochemical properties, delivering an exceptional specific capacity of 424.3 mAh $g^{-1}$ at 0.2 A $g^{-1}$, which is a significant improvement compared to $V_2O_5$ cathodes (Fig. 7a). More importantly, the cell maintains superior rate capability, exhibiting 122.5 mAh $g^{-1}$ even at a high current density of 1.0 A $g^{-1}$ (Fig. 7a). The galvanostatic charge–discharge profiles (Fig. 7b) reveal distinct voltage plateaus, indicating well-defined redox

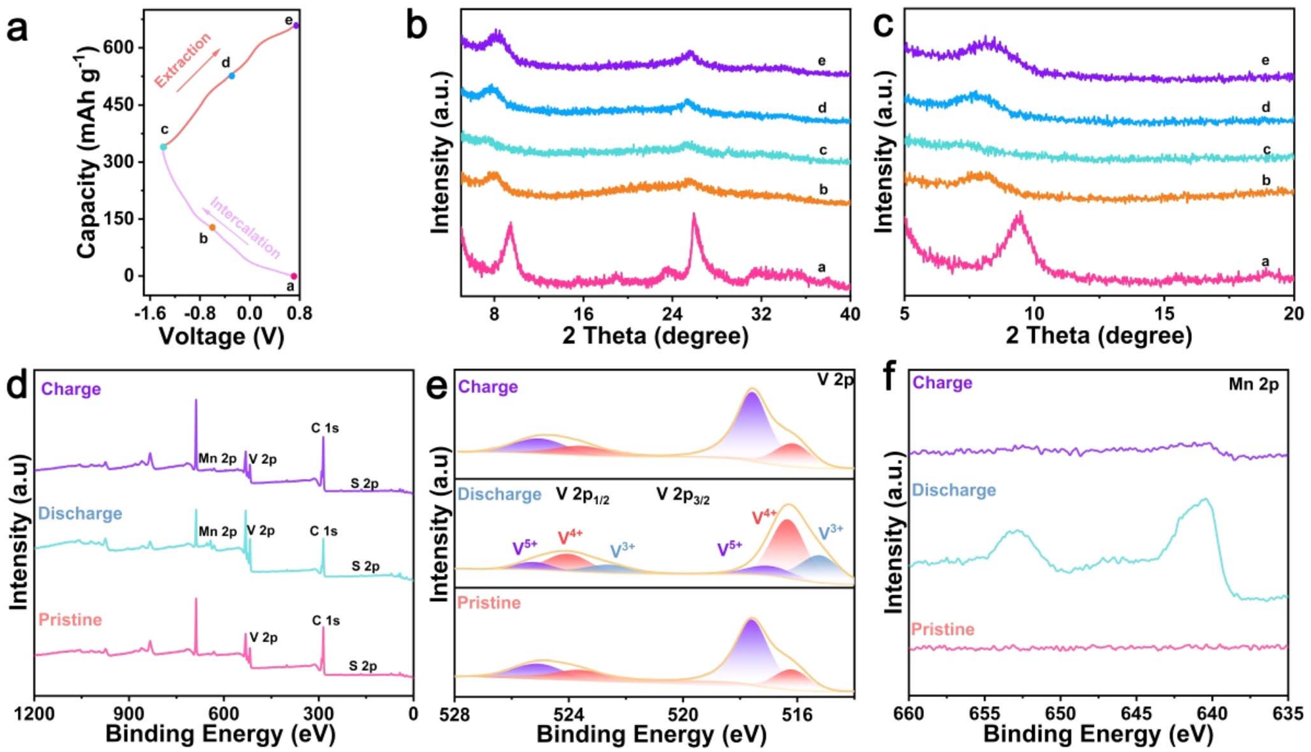


Fig. 5 (a) Charge–discharge profiles, (b) XRD curves, (c) magnified XRD curves, (d) XPS spectra, (e) V 2p spectra and (f) Mn 2p spectra of the $V_2O_5$@PEDOT composite at different discharged–charged states.

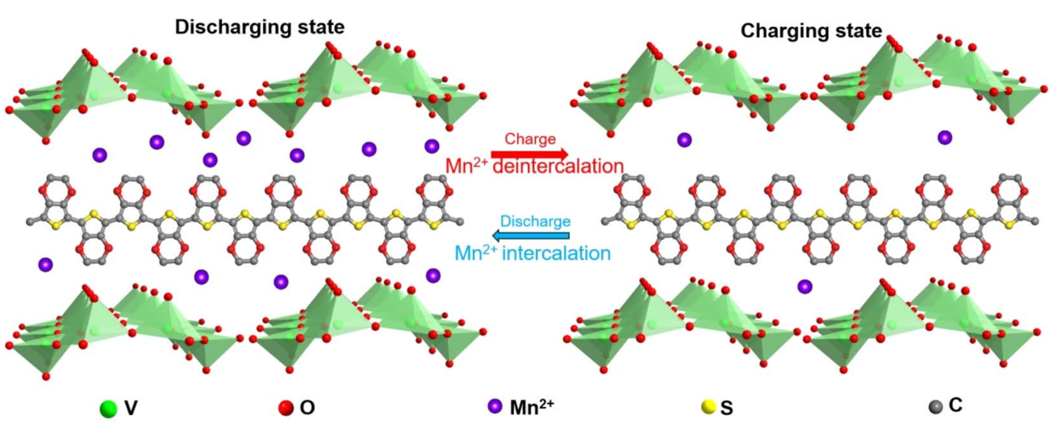


Fig. 6 Schematic of the storage mechanism of $Mn^{2+}$ ions.

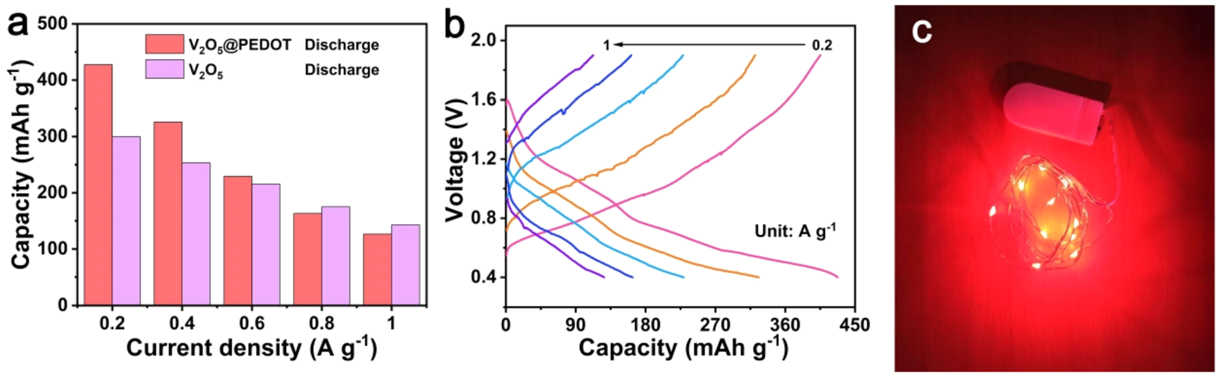


Fig. 7 (a) Capacity and (b) discharge–charge curves of the Mn||$V_2O_5$@PEDOT full cell at different current densities. (c) Optical image of the red LED lighted using two Mn||$V_2O_5$@PEDOT cells.

reactions during $Mn^{2+}$ insertion/extraction processes. To validate practical applicability, we successfully powered light-emitting diodes (LEDs) using two serially connected Mn||$V_2O_5$@PEDOT cells (Fig. 7c), demonstrating the real-world viability of this battery configuration. These results collectively highlight that the inorganic@organic $V_2O_5$@PEDOT nanocomposite is a promising cathode material for high-performance AMIBs.

## 4. Conclusions

The inorganic@organic $V_2O_5$@PEDOT nanocomposite was successfully synthesized *via* a facile *in situ* polymerization method by simply introducing the EDOT monomer into a $V_2O_5$ solution at room temperature, eliminating the need for additional oxidants or complex processing steps. The conformal PEDOT coating significantly enhanced the electrochemical performance by simultaneously suppressing vanadium dissolution and improving electronic conductivity, resulting in exceptional cycling stability after 1000 cycles at 5 A g$^{-1}$ in the $MnSO_4$ electrolyte and an exceptional rate capability (211.8 mAh g$^{-1}$ at 5 A g$^{-1}$). Systematic mechanism characterization confirmed the structural stability and high reversibility of $Mn^{2+}$ insertion/extraction. The practical applicability was further demonstrated in a full-cell configuration (Mn||$V_2O_5$@PEDOT), which maintained high capacity. This study not only presents a high-performance cathode material but also provides new insights into the design principles for advanced AMIBs, potentially expanding the research scope in sustainable energy storage systems.

## Data availability

All data supporting this research are included in the main article and ESI.†

## Author contributions

Xianyu Liu: conceptualization, writing original draft, and funding acquisition. Jianan Zhao: methodology, data curation, and validation. Zhigang Fan: writing – review & editing. Yingchun Xiao: supervision, investigation, and funding acquisition. Yande Zhao: formal analysis and resources. Qing Guo: investigation and validation.

## Conflicts of interest

The authors declare that they have no conflict of interest.

## Acknowledgements

This work is supported by the Natural Science Foundation of Gansu Province (No. 24JRRA538 & No. 25CXGA090), the Youth Doctoral Fund of Education Department of Gansu (No. 2025QB-085), the Discipline Construction Project of Lanzhou City University, the Talent Project of Rewi Alley and the Scientific Research Project of Lanzhou City University (No. LZCU-KJ/2024-017 & No. LZCU-KJ/2025-002).

## References

1 H. Wang, R. Tan, Z. Yang, Y. Feng, X. Duan and J. Ma, Stabilization Perspective on Metal Anodes for Aqueous Batteries, *Adv. Energy Mater.*, 2021, **11**, 2000962.
2 S. Chen, M. Zhang, P. Zou, B. Sun and S. Tao, Historical development and novel concepts on electrolytes for aqueous rechargeable batteries, *Energy Environ. Sci.*, 2022, **15**, 1805–1839.
3 X. Zhou, T. Ruan, J. Xu, C. Li, S. Huang, J. Zhou, S. Lu, R. Song and R. Li, Host-design strategies of zinc anodes for aqueous zinc-ion batteries, *RSC Adv.*, 2024, **14**, 23023–23036.
4 J. Pyun, H. Lee, S. Baek, S. Lee, H. Kwon, H. Lee, C. Y. Yoo and M. S. Chae, Nonaqueous Electrolyte Rechargeable Manganese Batteries with Potassium Manganese Hexacyanoferrate Cathodes, *Adv. Sci.*, 2025, 2500132.
5 S. Bi, Y. Zhang, S. Deng, Z. Tie and Z. Niu, Proton-Assisted Aqueous Manganese-Ion Battery Chemistry, *Angew. Chem., Int. Ed.*, 2022, **61**, e202200809.
6 Q. Yang, X. Qu, H. Cui, X. He, Y. Shao, Y. Zhang, X. Guo, A. Chen, Z. Chen, R. Zhang, D. Kong, Z. Shi, J. Liu, J. Qiu

and C. Zhi, Rechargeable Aqueous Mn-Metal Battery Enabled by Inorganic–Organic Interfaces, *Angew. Chem., Int. Ed.*, 2022, **61**, e202206471.

7 Z. Pan, T. Qin, W. Zhang, X. Chu, T. Dong, N. Yue, Z. Wang and W. Zheng, Non-layer-transformed $Mn_3O_4$ cathode unlocks optimal aqueous magnesium-ion storage via synergizing amorphous ion channels and grain refinement, *J. Energy Chem.*, 2022, **68**, 42–48.

8 Z. Fan, Z. Hou, W. Lu, H. Zheng, N. Chen, M. Yao, C. Wang, H. Jiang, D. Zhang and F. Du, Combination Displacement/Intercalation Reaction of $Ag_{0.11}V_2O_5$ Cathode Realizes Efficient Manganese Ion Storage Properties, *Small*, 2025, **21**, 2406501.

9 A. Nimkar, M. S. Chae, S. Wee, G. Bergman, B. Gavriel, M. Turgeman, F. Malchik, M. D. Levi, D. Sharon, M. R. Lukatskaya, N. Shpigel and D. Mandler, What About Manganese? Toward Rocking Chair Aqueous Mn-Ion Batteries, *ACS Energy Lett.*, 2022, **7**, 4161–4167.

10 S. Bi, S. Wang, F. Yue, Z. Tie and Z. Niu, A rechargeable aqueous manganese-ion battery based on intercalation chemistry, *Nat. Commun.*, 2021, **12**, 6991.

11 V. Soundharrajan, S. Nithiananth, J. Lee, K. Sakthiabirami, D. T. Pham, J. H. Kim, J.-Y. Hwang and J. Kim, Manganese ion batteries: $LiV_3O_8$ nanorods as a robust and long-life cathode module, *J. Power Sources*, 2023, **558**, 232542.

12 Z. Feng, J. Sun, Y. Liu, H. Jiang, T. Hu, M. Cui, F. Tian, C. Meng and Y. Zhang, Polypyrrole-intercalation tuning lamellar structure of $V_2O_5 \cdot nH_2O$ boosts fast zinc-ion kinetics for aqueous zinc-ion battery, *J. Power Sources*, 2022, **536**, 231489.

13 X. Zhang, F. Xue, X. Sun, T. Hou, Z. Xu, Y. Na, Q. An, Z. Chen, S. Cai and C. Zheng, High-capacity zinc vanadium oxides with long-term cyclability enabled by in-situ electrochemical oxidation as zinc-ion battery cathode, *Chem. Eng. J.*, 2022, **445**, 136714.

14 S. Cao, Y. Xiang, Q. Zou, Y. Jiang, H. Zeng, J. Li, J. Wu, X. Wu, X. Wu and L. Xiong, Preparation of $Li_3V_2(PO_4)_3$ as cathode material for aqueous zinc ion batteries by a hydrothermal assisted sol–gel method and its properties, *RSC Adv.*, 2023, **13**, 24385–24392.

15 C. Li, X. Yun, Y. Chen, D. Lu, Z. Ma, S. Bai, G. Zhou, P. Xiao and C. Zheng, Unravelling the proton hysteresis mechanism in vacancy modified vanadium oxides for High-Performance aqueous zinc ion battery, *Chem. Eng. J.*, 2023, **477**, 146901.

16 Z. Li, L. Yang, S. Wang, K. Zhu and H. Li, Co-insertion of $K^+$ and $Ca^{2+}$ in vanadium oxide as high-performance aqueous zinc-ion battery cathode material, *J. Alloys Compd.*, 2024, **992**, 174589.

17 Y. Du, Y. Wang, B. Yang, X. Liu, C. Li, W. Li, P. Zhang, H. Lu, D. Bin and Y. Xia, Mott–Schottky Heterojunction Modulating Iron–Vanadium Oxide for High-Performance Aqueous Zinc Battery Cathodes, *Nano Lett.*, 2025, **25**, 1002–1009.

18 W. Tang, Q. Li, H. Ren, Z. Gong, Q. Liu, J. Liang and W. Wu, Printed zinc ion battery with excellent rate performance utilizing carbon-intercalated vanadium oxide cathode for flexible wearable electronics, *J. Power Sources*, 2025, **640**, 236744.

19 S. Ye, S. Sheng, Q. Chen, L. Meng, W. Yao, H. Yao, Z. Wu and F. Zhang, Layer-by-layer assembled binder-free hydrated vanadium oxide-acetylene black electrode for flexible aqueous zinc ion battery, *J. Electroanal. Chem.*, 2024, **964**, 118334.

20 G. Yoo, Y.-G. Lee, B. Im, D. G. Kim, Y.-R. Jo and G. H. An, Integrated solution for a stable and high-performance zinc-ion battery using an electrolyte additive, *Energy Storage Mater.*, 2023, **61**, 102845.

21 C. Jia, X. Zhang, S. Liang, Y. Fu, W. Liu, J. Chen, X. Liu and L. Zhang, Environmentally adaptable hydrogel electrolyte with the triple interpenetrating network in the flexible zinc-ion battery with ultralong stability, *J. Power Sources*, 2022, **548**, 232072.

22 M. Wang, Y. Meng, Y. Xu, N. Chen, M. Chuai, Y. Yuan, J. Sun, Z. Liu, X. Zheng, Z. Zhang, D. Li and W. Chen, Aqueous all-manganese batteries, *Energy Environ. Sci.*, 2023, **16**, 5284–5293.

23 D. Bin, W. Huo, Y. Yuan, J. Huang, Y. Liu, Y. Zhang, F. Dong, Y. Wang and Y. Xia, Organic-Inorganic-Induced Polymer Intercalation into Layered Composites for Aqueous Zinc-Ion Battery, *Chem*, 2020, **6**, 968–984.

24 Y. Du, X. Wang and J. Sun, Tunable oxygen vacancy concentration in vanadium oxide as mass-produced cathode for aqueous zinc-ion batteries, *Nano Res.*, 2020, **14**, 754–761.

25 S. Li, X. Wei, C. Wu, B. Zhang, S. Wu and Z. Lin, Constructing Three-Dimensional Structured $V_2O_5$/Conductive Polymer Composite with Fast Ion/Electron Transfer Kinetics for Aqueous Zinc-Ion Battery, *ACS Appl. Energy Mater.*, 2021, **4**, 4208–4216.

26 T. Liu, Y. Liao, S. Liu, D. Tang, L. Chen and Q. Zhang, Understanding the Organic Intercalation for Aqueous Zinc-Ion Battery: From Interlayer Structure to Properties and Future Perspectives, *ACS Sustain. Chem. Eng.*, 2024, **12**, 15344–15369.

27 H. Qin, Z. Yang, L. Chen, X. Chen and L. Wang, A high-rate aqueous rechargeable zinc ion battery based on the $VS_4$@rGO nanocomposite, *J. Mater. Chem. A*, 2018, **6**, 23757–23765.

28 S. Zafar, M. Sharma, S. N. Mahapatra and B. Lochab, An aqueous zinc-ion battery with an organic–inorganic nanohybrid cathode featuring high operating voltage and long-term stability, *Chem. Commun.*, 2025, **61**, 3151–3154.

29 D. Xu, H. Wang, F. Li, Z. Guan, R. Wang, B. He, Y. Gong and X. Hu, Conformal Conducting Polymer Shells on $V_2O_5$ Nanosheet Arrays as a High-Rate and Stable Zinc-Ion Battery Cathode, *Adv. Mater. Interfaces*, 2019, **6**, 1801506.

30 A. Liu, F. Wu, Y. Zhang, Y. Jiang, C. Xie, K. Yang, J. Zhou and M. Xie, Ultralarge layer spacing and superior structural stability of $V_2O_5$ as high-performance cathode for aqueous zinc-ion battery, *Nano Res.*, 2023, **16**, 9461–9470.

31 M. Liu, X. Li, M. Cui, F. Chen, J. Li, W. Shi, Y. Liu, X. Li, Y. Wang, W. Zhang, C. Shao and Y. Liu, Amorphous organic-hybrid vanadium oxide for near-barrier-free ultrafast-charging aqueous zinc-ion battery, *Nat. Commun.*, 2024, **15**, 10769.

32 Y. Ren, S. Chen, M. Odziomek, J. Guo, P. Xu, H. Xie, Z. Tian, M. Antonietti and T. Liu, Mixing Functionality in Polymer Electrolytes: A New Horizon for Achieving High-Performance All-Solid-State Lithium Metal Batteries, *Angew. Chem., Int. Ed.*, 2025, **64**, e202422169.
33 Y. De Luna, Z. Mohamed, A. Dawoud and N. Bensalah, Innovative 2D dioxonium vanadium oxide: enhancing stability in aqueous zinc-ion battery cathodes, *RSC Adv.*, 2024, **14**, 39193–39203.
34 J. Xu, N. Han, S. Chen, Y. Zhang, Y. Jing, Z. Chen, S. Wang, R. Chen, P. Bing and Z. Li, The optimal integrating state of $VO_x$ with the synergistic effect of $Cu^{2+}$ cation and polyaniline for high performance flexible fiber zinc-ion battery, *J. Energy Storage*, 2025, **120**, 116415.
35 H. Ding, Y. He, X. Yu, L. Chen, M. Chen, Y. Luo, J. Li and S. Wei, A novel 3D framework loaded with $MnO_2$ for high-performance aqueous zinc-ion battery cathode, *J. Electroanal. Chem.*, 2025, **986**, 119101.
36 Y. Sha, J. Wang, Z. Sun, Z. Guo, J. Bi, H. Wang, C. Wang, Z. Liu and L. Qian, Sodium ion intercalated $NH_4V_4O_{10}$ with adjustable interlayer-spacing as an advanced cathode for aqueous zinc ion battery, *J. Energy Storage*, 2025, **114**, 115825.

 